Simultaneous Reconstruction of Activity and Attenuation in Time-of-Flight PET

Ahmadreza Rezaei[1], Michel Defrise[2], Girish Bal[3], Christian Michel[3], Maurizio Conti[3], Charles Watson[3], Johan Nuyts[1]

***Abstract*— In positron emission tomography (PET) and single photon emission tomography (SPECT), attenuation correction is necessary for quantitative reconstruction of the tracer distribution. Previously, several attempts have been undertaken to estimate the attenuation coefficients from emission data only. These attempts had limited success, because the problem does not have a unique solution, and severe and persistent "cross-talk" between the estimated activity and attenuation distributions was observed. In this paper, we show that the availability of TOF information eliminates the cross-talk problem by destroying symmetries in the associated Fisher information matrix. We propose a maximum-a-posteriori reconstruction algorithm for jointly estimating the attenuation and activity distributions from TOF PET data. The performance of the algorithm is studied with 2D simulations, and further illustrated with phantom experiments and with a patient scan. The estimated attenuation image is robust to noise, and does not suffer from the cross-talk that was observed in non-TOF PET. However, some constraining is still mandatory, because the TOF data determine the attenuation sinogram only up to a constant offset.**

I. INTRODUCTION

In nuclear medicine tomographic imaging (positron emission tomography (PET) and single photon emission tomography (SPECT)), a quantitative and artifact-free reconstruction of the tracer distribution can only be obtained if an accurate correction for the photon attenuation in the body of the patient is applied. The attenuation correction factors can be obtained from transmission measurements with radioactive sources, or be derived from well-aligned CT images [1]–[3]. Since both approaches have their limitations, several groups have attempted to jointly estimate the activity and attenuation images from the emission data only [4]–[12]. These attempts were based on the use of analytical consistency conditions, discrete consistency conditions and (penalized) maximum likelihood methods. Although some useful results have been obtained, the results have generally been disappointing. Nearly all studies report the so-called cross-talk problem, where localized errors in the activity image are compensated by localized errors in the attenuation image. This seems to be a fundamental problem. In the maximum-likelihood approach, the problem is manifested as the presence of local maxima in the likelihood function. However, in cases where incomplete information about the attenuation coefficients is available, these methods can be used to estimate the missing information, which is a less ill-posed problem than estimating the entire attenuation image [13]–[15].

Time-of-flight (TOF) Positron Emission Tomography (PET) was studied in the 1980's, but its implementation as a clinical instrument was too challenging at the time. Thanks to recent advances in electronics and in scintillation research, TOF PET has now been introduced in commercial systems [16]–[20]. The use of TOF information results in faster convergence of iterative reconstruction algorithms [21] and in an improved contrast-to-noise ratio [16], [22]. Moreover, recent studies have shown that in TOF PET, the artifacts induced by attenuation correction errors are less severe than in non-TOF PET [20]. This finding indicates that TOF PET data contain information about attenuation factors, that is not present in non-TOF PET data, justifying a study of the joint estimation problem in TOF PET.

In this paper, the simultaneous reconstruction of the activity and attenuation from TOF PET projections is studied as a maximum-likelihood problem, building on previous work for non-TOF emission computed tomography [7], [14]. In the following section this algorithm, Maximum Likelihood Activity and Attenuation estimation (MLAA), is briefly described. An analysis of the Fisher information matrix gives an intuitive explanation why local maxima in the form of cross-talk are a problem in non-TOF systems and why the use of TOF information eliminates this problem. However, the possible presence of other local maxima in the TOF likelihood needs further investigation. It is found that even with TOF PET the problem is still under-determined, i.e., TOF PET data determine the activity image up to a constant factor and the attenuation sinogram up to a (related) constant term. In the following section, some 2D simulation experiments are described and the results are presented. A 2D small scale simulation experiment was done to study the features of the Fisher matrix. 2D TOF PET simulations of a thorax phantom were done to study MLAA reconstructions with respect to the visual quality as a function of the TOF resolution, the constant factor/term and noise propagation. The stability of TOF-MLAA is studied numerically by starting the algorithms from a series of different initial images, including images containing cross-talk from the non-TOF MLAA reconstructions. The thorax phantom is also used to study bias and variance properties in a tissue region for MLEM and MLAA reconstructed emission images for multiple noise realizations. The method was applied to fully 3D TOF PET phantom scans and a patient scan, acquired on a commercial TOF PET system. Finally, the results of these 2D and 3D experiments are discussed in section IV.

---

[1] Nuclear Medicine, K.U.Leuven, B-3000 Leuven, Belgium. [2] Nuclear Medicine, Vrije Universitiet Brussel, B-1090 Brussels, Belgium. [3] Siemens Medical Solutions, MI, Knoxville, TN, USA.

[4]This research is supported by a research grant (GOA) from K.U.Leuven.

II. THEORY AND METHODS

A. MLAA

In TOF PET, the expected count $\bar{y}_{it}$ for line of response (LOR) i and time difference t can be expressed as follows:

$$\bar{y}_{it} = \sum_{j=1}^{J} c_{ijt} \lambda_j e^{-\sum_k l_{ik} \mu_k} + s_{it} \tag{1}$$

where λ_j and μ_k are the activity and attenuation coefficient at voxel j and k respectively, J is the total number of voxels, c_{ijt} is the sensitivity of the detector at (i, t) for activity in j in absence of attenuation, l_{ik} is the intersection length of LOR i with voxel k, and s_{it} is the expected contribution of scatter and/or randoms. Assuming that the data are Poisson distributed, the log-likelihood function can be written as

$$L(\theta, y_{it}) = \sum_{it} y_{it} \ln \bar{y}_{it} - \bar{y}_{it} \tag{2}$$

where y_{it} is the measured count at (i, t) and $\theta = [\lambda^T, \mu^T]^T$ is the set of $2J$ parameters that has to be estimated. Note that summation over the TOF index (t) yields the corresponding non-TOF values, which are denoted by omitting the index t: $\sum_t c_{ijt} = c_{ij}$, $\sum_t y_{it} = y_i$ and $\sum_t s_{it} = s_i$.

The MLAA algorithm uses an interleaved updating: in every iteration first the activity is updated keeping the attenuation coefficients constant, and then vice versa. This can be written as follows:

$$\begin{aligned}
\forall i: \quad a_i^h &= e^{-\sum_j l_{ij} \mu_j^h} && (3)\\
\forall j: \quad \lambda_j^{h+1} &= \frac{\lambda_j^h}{\sum_{it} a_i^h c_{ijt}} \sum_{it} a_i^h c_{ijt} \frac{y_{it}}{\sum_\xi a_i^h c_{i\xi t} \lambda_\xi^h + s_{it}} && (4)\\
\forall i: \quad \psi_i^h &= a_i^h \sum_{jt} c_{ijt} \lambda_j^{h+1} && (5)\\
\forall j: \quad \mu_j^{h+1} &= \mu_j^h + \frac{\sum_i l_{ij} \frac{\psi_i^h}{\psi_i^h + s_i} (\psi_i^h + s_i - y_i)}{\sum_i l_{ij} \frac{(\psi_i^h)^2}{\psi_i^h + s_i} \sum_\xi l_{i\xi}} && (6)
\end{aligned}$$

where the superscript h denotes the iteration number. The non-TOF sinogram a^h represents the attenuation computed from the current estimate μ^h, and the non-TOF sinogram elements ψ_i^h represent the expected TOF-integrated count for LOR i, but without the additive contribution s_i. Expression (4) is a standard Maximum Likelihood Expectation Maximization (MLEM) iteration [23], which makes explicit use of the TOF PET data. Expression (6) is the Maximum Likelihood for Transmission tomography (MLTR) update [24], [25], which only uses the TOF-integrated data. Note that the sinogram with elements $\sum_{jt} c_{ijt} \lambda_j^{h+1}$ plays the role of the blank scan, while the TOF integrated data y_i are treated as the transmission scan.

Both MLEM and MLTR can be accelerated with ordered subsets. Furthermore, because the TOF information improves convergence of MLEM but not that of MLTR, we typically cycle through the subsets faster for the MLTR updates (using the same subsets definition for both). Thus, for every MLEM update $N \geq 1$ MLTR updates are done, and when all projections have contributed once to the activity updates, they have contributed N times to the attenuation updates. This decreases the processing time considerably, also because the MLTR updates only involve non-TOF projections and backprojections. Unless otherwise stated, $N = 5$.

B. The curvature of the likelihood

In [26] it has been shown that for TOF PET, the joint estimation problem has a unique solution, except for a constant scale factor. However, this result does not exclude the existence of local maxima in the TOF likelihood function. Convergence to a global maximum would be guaranteed provided that the matrix of second derivatives of the TOF likelihood with respect to the complete parameter space, θ, were negative definite. Although the log-likelihood function is known to be concave with respect to λ or μ, so far we have not been able to prove concavity with respect to θ.

If the algorithm is started with initial images sufficiently close to the true solution, then any gradient ascent algorithm should converge to the global maximum of the likelihood, even in the presence of (distant) local maxima. Therefore, it is meaningful to study the stability of the ML-algorithm close to the true solution. This stability is determined by the curvature of the likelihood. In the following, we study that curvature for both TOF and non-TOF systems. It is shown that close to the true solution, other possible solutions still exist for the non-TOF case (commonly referred to as cross-talk) whereas these solutions are eliminated with the introduction of TOF information.

In our analysis we ignore the non-negativity constraint and the scatter/randoms contributions, assume the likelihood has been maximized and then look for a small change $\Delta\theta$ that does not change the gradient of the likelihood. If such a $\Delta\theta$ can be found, then both θ and $\theta + \Delta\theta$ maximize the likelihood, implying that the problem is under-determined. A small $\Delta\theta$ does not change the gradient of the likelihood if it satisfies the following equation:

$$\sum_k \frac{\partial^2 L}{\partial\theta_j \partial\theta_k} \Delta\theta_k = 0, \quad j = 0, ..., 2J \tag{7}$$

Since we are at the likelihood maximum, we make the approximation that the second derivative of the likelihood can be replaced by its expectation, equal to minus the Fisher information matrix (FIM) [27], [28]. Equation 7 then becomes:

$$F \Delta\theta = 0 \tag{8}$$

where, F is the $2J \times 2J$ FIM and $\Delta\theta$ is the $2J \times 1$ matrix representing the change in the parameter space.

Replacing θ with $[\lambda^T, \mu^T]^T$, the Fisher information matrix can be rewritten in a quadrant form as follows

$$\begin{aligned}
F &= -E[\frac{\partial^2 L}{\partial\theta \partial\theta}]\\
&= \begin{pmatrix} -E[\frac{\partial^2 L}{\partial\lambda \partial\lambda}] & -E[\frac{\partial^2 L}{\partial\lambda \partial\mu}] \\ -E[\frac{\partial^2 L}{\partial\mu \partial\lambda}] & -E[\frac{\partial^2 L}{\partial\mu \partial\mu}] \end{pmatrix} = \begin{pmatrix} F_{\lambda\lambda} & F_{\lambda\mu} \\ F_{\lambda\mu}^T & F_{\mu\mu} \end{pmatrix} && (9)
\end{aligned}$$

where E is the expectation operator and for all $j, k = 1, \ldots, J$ combinations,

$$\begin{aligned}
-E[\frac{\partial^2 L}{\partial \lambda_j \partial \lambda_k}] &= \sum_{i,t} \frac{c_{ijt} c_{ikt}}{\bar{y}_{it}} e^{-2\sum_\xi l_{i\xi}\mu_\xi} \qquad (10)\\
-E[\frac{\partial^2 L}{\partial \mu_j \partial \mu_k}] &= \sum_{i,t} l_{ij} \bar{y}_{it} l_{ik} = \sum_i l_{ij} \bar{y}_i l_{ik}, \qquad (11)\\
-E[\frac{\partial^2 L}{\partial \lambda_j \partial \mu_k}] &= -\sum_{i,t} c_{ijt} l_{ik} e^{-\sum_\xi l_{i\xi}\mu_\xi}\\
&= -\sum_i c_{ij} l_{ik} e^{-\sum_\xi l_{i\xi}\mu_\xi}. \qquad (12)
\end{aligned}$$

Replacing $\Delta\theta$ with $[\Delta\lambda^T, \Delta\mu^T]^T$, (8) becomes

$$\begin{pmatrix} F_{\lambda\lambda} & F_{\lambda\mu} \\ F_{\lambda\mu}^T & F_{\mu\mu} \end{pmatrix} \begin{pmatrix} \Delta\lambda \\ \Delta\mu \end{pmatrix} = 0 \tag{13}$$

$F_{\lambda\lambda}$ is expected to be invertible, because the reconstruction of the activity is fairly stable when the attenuation is fixed. If $F_{\lambda\lambda}$ is indeed invertible, then $\Delta\lambda$ can be eliminated, yielding

$$(F_{\mu\mu} - F_{\lambda\mu}^T F_{\lambda\lambda}^{-1} F_{\lambda\mu}) \Delta\mu = 0. \tag{14}$$

In the following, we show that for non-TOF systems, and in particular near the center of uniform objects, the operators $F_{\mu\mu}$, $F_{\lambda\mu}$ and $F_{\lambda\lambda}$ are all very similar, such that the equation is expected to be (almost) satisfied for many possible local changes $\Delta\mu$. The corresponding $\Delta\lambda$ that results in cross-talk can be computed from (13). The incorporation of TOF information changes the operator $F_{\lambda\lambda}$, such that (14) no longer has solutions for local changes $\Delta\mu$.

Inserting (10)-(12) into (13) yields

$$\begin{aligned}
\sum_{kit} \frac{c_{ijt} c_{ikt}}{\bar{y}_{it}} e^{-2\sum_\xi l_{i\xi}\mu_\xi} \Delta\lambda_k &= \sum_{ki} c_{ij} l_{ik} e^{-\sum_\xi l_{i\xi}\mu_\xi} \Delta\mu_k\\
\sum_{ki} l_{ij} c_{ik} e^{-\sum_\xi l_{i\xi}\mu_\xi} \Delta\lambda_k &= \sum_{ki} \bar{y}_i l_{ij} l_{ik} \Delta\mu_k \qquad (15)
\end{aligned}$$

For the non-TOF case, the TOF index t must be dropped, and the first equation in (15) becomes:

$$\sum_{ki} \frac{c_{ij} c_{ik}}{\bar{y}_i} e^{-2\sum_\xi l_{i\xi}\mu_\xi} \Delta\lambda_k = \sum_{ki} c_{ij} l_{ik} e^{-\sum_\xi l_{i\xi}\mu_\xi} \Delta\mu_k$$

The coefficients c_{ij} and l_{ij} both represent the contribution of pixel j to the acquisition along LOR i and should have very similar values. Assuming they are identical except for a factor (which can be absorbed in λ or μ by changing the units), the non-TOF equations become:

$$\begin{aligned}
\sum_i l_{ij} \frac{e^{-\sum_\xi l_{i\xi}\mu_\xi}}{\bar{y}_i} \sum_k l_{ik} (e^{-\sum_\xi l_{i\xi}\mu_\xi} \Delta\lambda_k - \bar{y}_i \Delta\mu_k) &= 0\\
\sum_i l_{ij} \sum_k l_{ik} (e^{-\sum_\xi l_{i\xi}\mu_\xi} \Delta\lambda_k - \bar{y}_i \Delta\mu_k) &= 0 \qquad (16)
\end{aligned}$$

An extreme case is obtained when the attenuation corrected counts $\bar{y}_i e^{\sum_\xi l_{i\xi}\mu_\xi}$ are constant for all LORs i that intersect the region where $\Delta\lambda$ is non-zero. In that case, the two sets of equations in (16) become identical and will have non-zero solutions. For example, if one considers a small change at a single pixel k, the solution equals

$$\frac{\Delta\lambda_k}{\Delta\mu_k} = \bar{y}_i e^{\sum_\xi l_{i\xi}\mu_\xi}. \tag{17}$$

The use of time-of-flight changes the elements of the submatrix $F_{\lambda\lambda}$ in the Fisher information matrix, destroying the similarity between the two equations. As a result, pixel-by-pixel cross-talk becomes impossible. However, the existence of other possible local maxima of the likelihood still needs to be thoroughly analyzed.

C. *Uniqueness of the solution*

The analysis above indicates that TOF information eliminates high-frequency cross-talk between the emission and attenuation reconstructions in the joint estimation. However, it does not exclude low-frequency cross-talk. In our experiments, we observed that MLAA produces images that are visually free of artifacts, but differ from the true images by a scale factor. Here we attempt to gain some insight in this scaling effect, by deriving a scaled solution from the true image. Suppose the images $[\lambda, \mu]$ maximize the likelihood. If we multiply λ with a constant, the computed sinogram $\bar{y}$ eq. (1) is multiplied with the same constant. We show that we can always increase the attenuation image μ to compensate for that change, such that we obtain an alternative solution that produces the same $\bar{y}$ and therefore the same (maximum) likelihood.

Assume that the true tracer distribution is λ^o and the true attenuation image is μ^o. The sinogram attenuation factors due to the attenuation image μ^o equal $\exp(-P\mu^o)$, where P is the non-TOF projection operator. Consequently, the attenuated emission sinogram (without the scatter/randoms contributions) equals $\bar{y} = (P_t\lambda^o) * \exp(-P\mu^o)$, where P_t is the TOF projector operator. We also assume that λ^o and μ^o have a finite support S, meaning $\lambda_j^o = 0$ and $\mu_j^o = 0$, $\forall j \notin S$, where j is the voxel index.

Define a sinogram region Ω as the set of lines of response that contain activity (the projection of S produces this sinogram region). Now consider a non-TOF sinogram U which is uniform within the sinogram region Ω:

$$U_i = \ln(\alpha), \quad \forall i \in \Omega$$

where i is the sinogram index, $\alpha > 0$ and sinogram U is allowed to have any values outside Ω. Consistent sinograms satisfying the above condition can be found so there exists an image μ^α such that inside Ω we have $U = P\mu^\alpha = \ln(\alpha)$ and hence $\exp(-P\mu^\alpha) = 1/\alpha$. Thus, the attenuation created by the modified attenuation image $(\mu^o + \mu^\alpha)$ equals $P\mu^o/\alpha$. It follows that sinogram $\bar{y}$ can also be obtained with activity image $\alpha\lambda^o$ and attenuation image $\mu^o + \mu^\alpha$, for any α where $\mu^o + \mu^\alpha \geq 0$. Note that with this construction, the activity is globally scaled while the attenuation undergoes a position dependent scaling.

Interestingly, when the sinogram region Ω is known exactly and the attenuation values are set to zero outside this region:

$$U_i = \begin{cases} \ln(\alpha), & \forall i \in \Omega \\ 0. & \forall i \notin \Omega \end{cases}$$

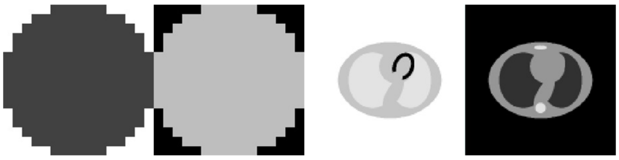

Fig. 1. Activity and attenuation images of the simulated phantoms: left: the 16x16 pixels phantom to study the Fisher information matrix, right: the 2D thorax phantom.

sinogram U can no longer be expressed by a projection of a bounded attenuation image μ^α. This is due to the singularities in μ^α present at the boundaries of S making it unlikely for any joint estimation reconstruction to reach a scaled solution of the true images. This would imply that the solution of joint estimation is truly unique with a known object boundary. However, our first experiments indicate that the practical value of this argument is questionable, because small errors in the object's boundary seem to be enough to reintroduce the scaling problem.

In [26], this problem is studied based on a consistency condition for 2D TOF PET data. It was shown there that the set of scaled solutions $\{\alpha\lambda^o, \mu^o + \mu^\alpha : \alpha > 0\}$ described above are the only solutions to the joint estimation problem from TOF PET emission data. Thus, it will still be necessary to use some a-priori knowledge about the expected intensities of the activity and/or the attenuation images. In most cases, the most convenient will be to use a-priori values for the attenuation in tissue.

III. EXPERIMENTS

In the following figures, the activity images will be shown in a white-to-black color map whereas a black-to-white color map will be used to show the attenuation images.

A. 2D Simulations

Figure 1 shows the two phantoms used in our 2D phantom studies. We use a Field-of-View (FOV) of 40 cm for the study of the features of the FIM and the study of visual quality of the reconstructions as a function of time resolution and iterations. For the study of the influence of different initializations on the induced constant factor/term, noise propagation and bias and variance in emission reconstructions more realistic TOF specifications adjusted to commercially available TOF PET systems will be used.

1) The Fisher information matrix: In this study, the 16×16 circular phantom shown in figure 1 with uniform activity and uniform tissue attenuation was used. For this toy problem, the Fisher information matrix can be computed explicitly because its size is only 512×512. Non-TOF submatrices of the Fisher information matrix were compared to a TOF system with a spatial resolution of 2.5 cm FWHM corresponding to a pixel resolution. These submatrices, $F_{\lambda\lambda}, F_{\lambda\mu}$ and $F_{\mu\mu}$, are considered as operators and their impulse response is computed for the pixel located near the center of the FOV.

Figure 2 shows the central row of each of the FIM submatrices defined in (9) reshaped into the size of the emission and attenuation images. It should be noted that since only the first term of the FIM incorporates both TOF projection and TOF backprojection operators, the elements of this first term, $F_{\lambda\lambda}$, change for a TOF system while the other three terms remain unchanged.

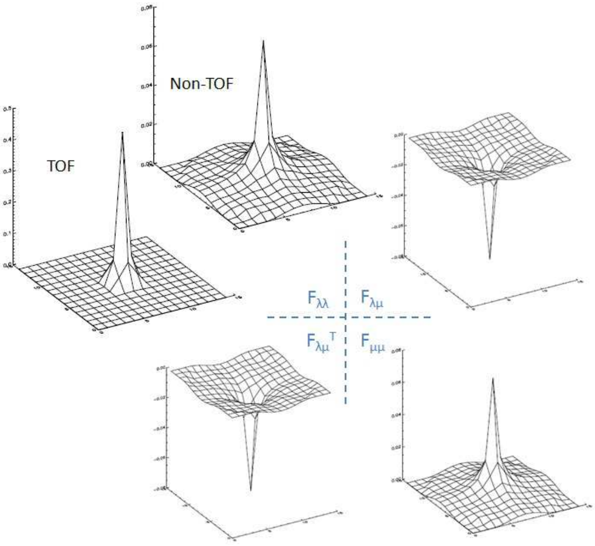

Fig. 2. The four Fisher Information PSFs for a change in the emission/attenuation of the pixel located near the center of the FOV. Top-left: the effect of emission change in the emission image for a TOF and a non-TOF system, top-right: the effect of attenuation change seen in the emission image, bottom-left: the effect of emission change seen in the attenuation image and vice versa, bottom-right: the effect of attenuation change seen in the attenuation image.

The top left figures show the FIM response in the emission image for a small change of the activity in the pixel located close to the center of the FOV, for both TOF and non-TOF systems. The top right and bottom left figures show the influence of a small change in the attenuation and activity of the central pixel seen in the emission and attenuation images respectively. The bottom right figure shows the effect of a change in the attenuation image for a change of attenuation for the same pixel. Using the term Point Spread Function (PSF) with caution[1], figure 2 shows the four PSFs for the pixel in the center of the FOV.

It can be seen from figure 2 that the four PSFs of a non-TOF system are very similar. Comparing this to the system of equations (13), it can be seen that for some simultaneous change in the emission and attenuation values of the central pixel, these changes can potentially cancel each other out (as long as they don't violate the non-negativity constraint). Hence, these changes can not be identified from the measurements because they do not modify the value of the likelihood, which remains at its maximum. On the other hand, for a TOF system the four PSFs are no longer similar. Thus, a change in the activity of a pixel can no longer be compensated by a change in the attenuation of the same pixel, which makes activity and attenuation cross-talk impossible.

2) Thorax Phantom: For the 2D thorax phantom shown in fig 1, 2D sinograms with 128 detectors (bin size 3.125

---

[1] position dependant PSF in the FIM

mm), 128 projection angles over 180 degrees and a TOF sampling density of at least $4/\text{FWHM}_{\text{TOF}}$ were generated. An oversampling of 3 was used during simulation (i.e. 3 rays per LOR, 9 subpixels per image pixel) to account for slight mismatch between the simulation and reconstruction projectors and the reconstructed images had 128×128 pixels. The emission data provide no attenuation information about LORs that do not intersect the activity distribution. Therefore, MLAA was applied with a penalty that is active only for the voxels located outside the body contour and inside the body contour, no priors were applied. In that external region, we use a penalty that favors zero attenuation values outside that body contour. We find an estimate of the object boundary by thresholding either the sinogram or the initial reconstruction and outside this boundary the intensity prior was set to have a negative derivative for any pixel value, except for zero and tissue attenuation (in which case the derivative was zero). The addition of this prior, modifies the MLTR update step of eq. (6) by the addition of the prior gradient and its second derivative to the numerator and the denominator, respectively. Details of the prior are provided in the appendix.

To study the effect of TOF resolution on image quality, simulations were conducted for multiple TOF resolutions varying from 40 cm (approximately non-TOF) to 2.5 cm corresponding to time resolutions of 2667 ps to 167 ps. Simultaneous activity and attenuation images were reconstructed varying the number of iterations to study the convergence properties. For these experiments the attenuation image was initialized by filling the correct body contour uniformly with tissue attenuation and a uniform activity within the FOV was used as the initial activity image.

Figure 3 shows the resulting activity and attenuation reconstructions of the noiseless thorax phantom after 5, 15 and 50 iterations of MLAA for varying TOF resolutions. In this study the attenuation images were updated only once for each update of the activity (N=1).

It can be seen from figure 3 that, after 50 iterations of MLAA the estimated activity and attenuation images for a TOF resolution of 40 cm FWHM still suffer from cross-talk and have not visually converged to the true images. When the TOF resolution is improved to 20 cm FWHM, the reconstructions after 50 iterations improve significantly, but they still differ from the true images. For TOF resolutions below 20cm FWHM the reconstructions visually converge to the true image. However, the reconstructions differ from the true images by a scaling factor which can not be seen here. It can also be seen that as the TOF resolution increases the speed of convergence increases as well.

Next, the simulation specifications were adjusted according to the Siemens Biograph scanner specifications [19]. For the 2D thorax phantom shown in fig 1, 2D sinograms with 200 detectors (bin size 4.01 mm) and 168 projection angles over 180 degrees were generated. An effective TOF resolution of 580 ps (= 8.7 cm) FWHM and a time-bin width of 312 ps were used to generate the sinograms. This time-bin width of 312 ps is sufficient to avoid aliasing artifacts in the reconstructed image [29]. However, it results in an effective broadening of the TOF FWHM, which can have an impact on the speed of convergence. Our simulations indicate that this effect is negligible. We used an oversampling of 3 during simulations, the reconstructed images had 200×200 pixels and as before MLAA with a penalty that is only active outside the body contour was used. The following MLAA reconstructions are after 3 iterations of 42 subsets with N=5.

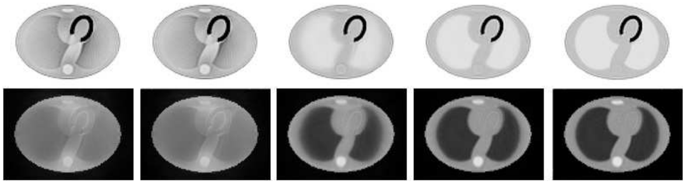
a) After 5 iterations

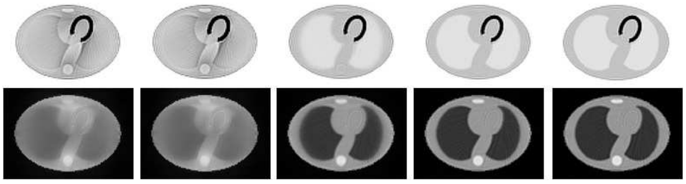
b) After 15 iterations

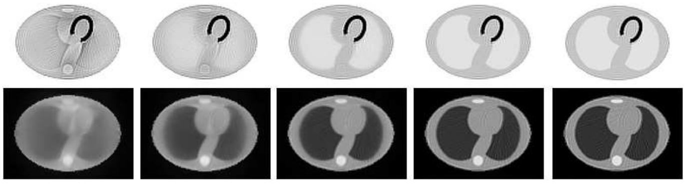
c) After 50 iterations

Fig. 3. Activity and attenuation reconstructions after 5, 15 and 50 iterations and 32 subsets of MLAA for TOF resolutions of 40 cm (approximately non-TOF), 20 cm, 10 cm, 5 cm and 2.5 cm.

To study the effect of different initializations on the final MLAA reconstructions, initial attenuation images with the correct body contour were filled with 0.5, 1 and 2 times tissue attenuation. A zero image, a smooth image with attenuation concentrated at the center, an image with random noise and an image designed to encourage cross-talk near the heart were also used for this purpose. We found that the MLAA reconstructions converged to very similar images that differed from the true image just by a scale factor. Each of these initialization images produced a different scale factor in the final reconstruction image but apart from this the reconstructions were cross-talk free and comparable to the true activity and attenuation images.

Figure 4 shows a few of the initial images used in this study together with their final TOF-MLAA reconstructions. The final reconstructions shown in figure 4 show no sign of activity and attenuation cross-talk. However the final activity reconstructions appear in different shades which is due to the scale factor which the activity reconstructions differ by from the true activity distribution. The right most initializations used in figure 4 was produced by a non-TOF MLAA reconstruction to encourage cross-talk in the activity and attenuation images. As with all other initial images used, after sufficient iterations of the algorithm, the reconstructions visually converged to the true image, but differed by a scale factor. This indicates that TOF-MLAA is able to get rid of any cross-talk which might be already present in the initial images.

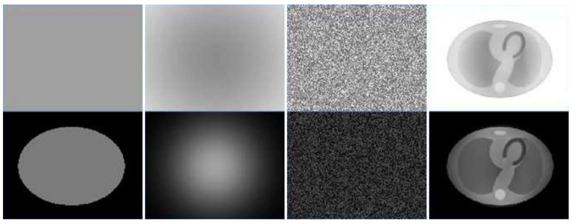

a) Initial activity (top) and attenuation (bottom) images.

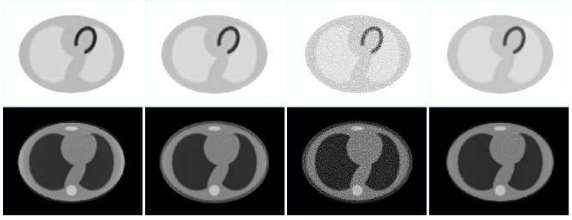

b) Final activity (top) and attenuation (bottom) reconstructions.

Fig. 4. Initial activity and attenuation (top) images and their respective TOF-MLAA activity and attenuation reconstructions (bottom). Initial images from left to right: uniform attenuation within the body contour filled with tissue attenuation, smooth attenuation image with attenuation concentrated at the center, initial images filled with random noise and a non-TOF MLAA reconstruction image designed to encourage cross-talk.

Poisson noise was then added to the sinogram of the 2D thorax phantom to analyze the behaviour of MLAA under noisy conditions. The maximum count in the sinogram was chosen to be less than 10. The activity and attenuation images were reconstructed from this noisy sinogram starting from uniform initial images. As reference images, we used the MLEM reconstruction of the activity using the true attenuation coefficients and the MLTR reconstruction of the attenuation using the true activity distribution. The same experiment was repeated for a noise-free sinogram. We assume that the resulting noise-free reconstruction is a good estimate of the mean over many noise realizations. From these images, noise correlation coefficients (NCC) were computed between the MLAA reconstructions ($\mathcal{M}$) and the reference reconstructions ($\mathcal{R}$) as,

$$NCC = \frac{\sum_j (\mathcal{M}_j^n - \mathcal{M}_j^f)(\mathcal{R}_j^n - \mathcal{R}_j^f)}{\sqrt{\sum_j (\mathcal{M}_j^n - \mathcal{M}_j^f)^2 \sum_j (\mathcal{R}_j^n - \mathcal{R}_j^f)^2}}, j = 1, ..., J \tag{18}$$

where subscript j determines the pixel index and superscripts n and f determine the noisy and the noise-free reconstructions respectively.

Figure 5 compares the MLAA reconstructions from a noisy sinogram to the reference images computed from MLEM and MLTR reconstructions, revealing strong noise correlations. A noise correlation coefficients of 0.86 was computed for the MLAA reconstructed activity image starting from uniform initial images with respect to the MLEM reconstructed activity image with known attenuation. The same measure was computed to be 0.92 for the MLAA reconstructed attenuation image with respect to the MLTR reconstructed attenuation image with known activity. This high noise correlation suggests that TOF simultaneous reconstruction handles noise just as reconstructions from known activity or attenuation images. Apparently, the noise in the sinogram does not propagate to make simultaneous reconstructions unstable.

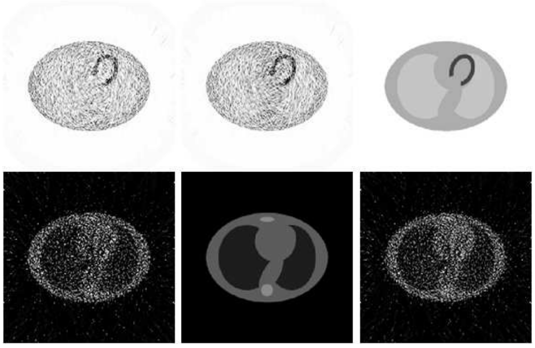

Fig. 5. Activity (top) and attenuation (bottom) images reconstructed from a noisy sinogram. The reconstructed results of MLAA initialized by uniform images (left) are compared to that of an MLEM (center) and MLTR (right) with known attenuation and activity images respectively.

With more realistic noise in the emission data, we study bias and variance in the MLEM and MLAA emission reconstructions as a function of reconstruction updates. We presume that an estimate of the scale in the attenuation-corrected emission sinogram is available and we plot the bias and variance curves for a 4.5 cm diameter region-of-interest (ROI) in a tissue region of the thorax phantom shown in figure 6. The bias is then computed in each reconstruction update for 100 different noise realizations as the relative difference of the ROI values to the true ROI values of the thorax phantom. Figure 6 shows the bias and variance curves in the ROI for 200 MLEM and MLAA updates of the emission image. The marked points on the curves correspond to bias and variance values after 20 emission updates, i.e. updates 20, 40, 60, ..., 200. We do not use subsets in this study and as before N=5.

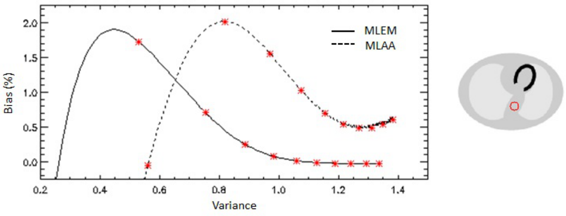

Fig. 6. Bias and variance curves (left) in the MLEM and MLAA reconstructed emission images as a function of reconstruction updates for a 4.5 cm diameter ROI shown in red (right). The marked points on the curves show bias and variance values for 20 updates of the emission image which are computed from 100 different noise realizations.

Figure 6 shows that the MLEM reconstructions outperform the MLAA reconstructions, yielding a lower bias at the same variance level. This observation is expected since MLEM uses a known attenuation, whereas MLAA estimates both the emission and the attenuation. Comparison between the marked points on the two curves (at every 20 iterations) indicates that MLEM also converges faster than MLAA. The left end of the curves correspond to unreliable transient values of bias and variance at the first few updates of the reconstructed emission image.

B. Phantom scans and patient study

A fully 3D implementation of MLAA has been applied to two phantom scans and a clinical patient study. The scans have been acquired on a Siemens Biograph mCT system [19]. The TOF PET data are organized as 5D sinograms, consisting of 400 radial bins, 168 azimuthal angles, 9 co-polar angles, up to 109 planes (depending on the co-polar angle) [30], and 13 time bins of 312 ps width, with an effective TOF resolution of 580 ps. The patient bore of the scanner is 78 cm with a PET field-of-view of 69 cm, which makes truncation an issue for big phantoms or patients.

By simple thresholding and backprojection operations, a reasonable estimate of the body contour can be obtained [7]. In order to deal with the scale problem in the MLAA reconstructions, we impose the known value of tissue attenuation to the 75^{th} percentile of the attenuation value within this (initial) body contour. This value is imposed by scaling the entire attenuation image. The scale factor required to insure tissue attenuation rapidly converges to 1. For the images considered here, the 75^{th} percentile corresponded to tissue, but of course, more sophisticated segmentation algorithms could be used for this purpose. Outside the body contour however, the same background prior as described above and in the appendix was used to encourage background attenuation values to become zero. In both 3D studies, the smoothing relative difference prior of [31] was also used to encourage smoothness in the attenuation images.

1) 3D Phantom Study: The NEMA IEC body phantom [32] was used to evaluate the simultaneous activity and attenuation reconstructions in 3D. The measurements corresponded to a 5 minute scan of 229 MBq injection scanned 2 hours post-injection. The phantom was located once in the center of the FOV and once closer towards the edge of the FOV. In this study, the contributions of scatter were not taken into account and we did not try to enforce bed attenuation in the attenuation image.

Results from 3D reconstructions of activity and attenuation of the NEMA IEC body phantom located near the FOV center of the mCT are shown in figures 7 and 8. The reconstructions are shown for two different transaxial planes: one having more details in the activity image, figure 7, and one with more details in the attenuation image, figure 8. The MLAA reconstructions are compared to the CT-based attenuation image and the OSEM reconstructions of the activity with CT-based attenuation correction. The reconstructions shown here are from 3 MLAA iterations of 42 subsets.

The TOF-MLAA reconstructions do not suffer from activity and attenuation cross-talk. However because we did not correct for scatter, slight activity is present within the cavity of the NEMA phantom and some excess attenuation around the object of interest. It can also be seen in figure 8 that the algorithm has tried to compensate for bed attenuation by putting attenuation values outside the boundary of the object. Using the CT-based scatter estimate [33] and bed attenuation during MLAA reconstructions, activity and attenuation images were reconstructed free of these artifacts, however, the results are not shown here. Similar results were also obtained for the phantom in the off-center position.

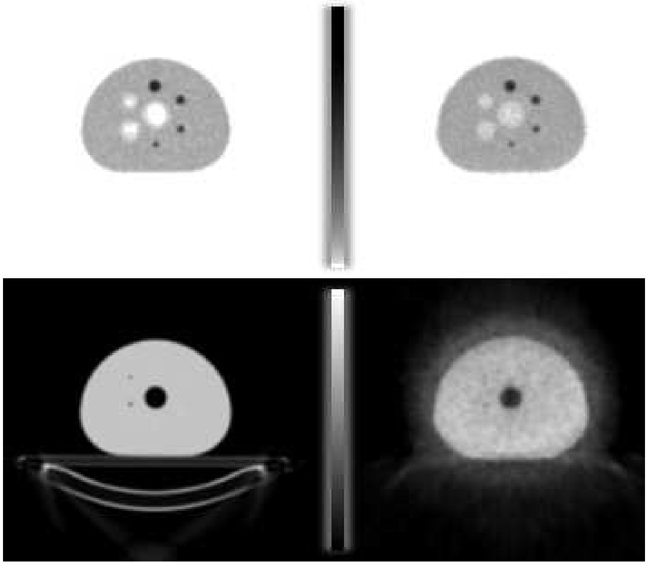

Fig. 7. CT attenuation corrected MLEM reconstructions (top-left), FBP attenuation reconstruction of the CT (bottom-left), MLAA reconstructed emission (top-right) and attenuation (bottom-right) images of the 3D NEMA phantom located near the center of the FOV. The vertical bars represent the gray level lookup table for activity and attenuation.

2) Clinical study: A clinical five minute scan of the thorax of a patient injected with 570 MBq ^{18}F-FDG was used to reconstruct the activity and attenuation images. Due to the patient size, the TOF PET measurements suffer from truncation near the edge of the FOV of the system. As shown

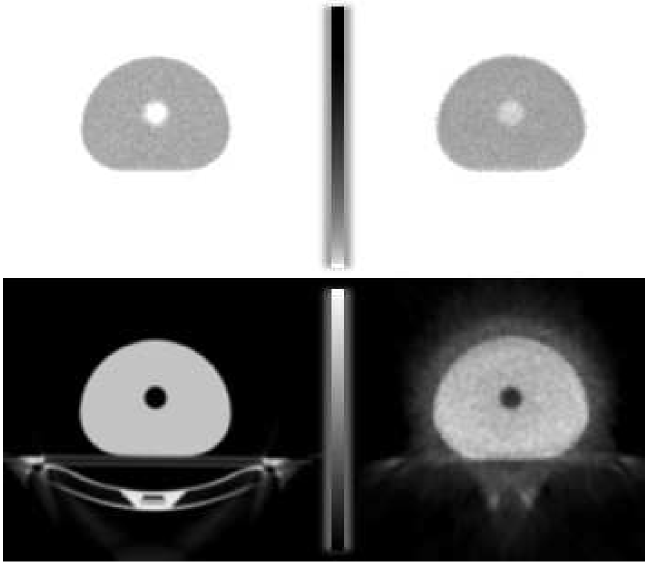

Fig. 8. CT attenuation corrected MLEM reconstructions (top-left), FBP attenuation reconstruction of the CT (bottom-left), MLAA reconstructed emission (top-right) and attenuation (bottom-right) images of the 3D NEMA phantom located near the center of the FOV. The vertical bars represent the gray level lookup table for activity and attenuation.

below, the truncation affected the reconstruction of the arms in the PET and CT images, as well as in the MLAA images. Two different MLAA reconstructions were computed. For the first reconstruction, we used the precomputed CT scatter estimate and imposed the CT-based bed attenuation in the attenuation image. This reconstruction illustrates the effectiveness of TOF data for joint activity and attenuation estimation in ideal situations. In the second reconstruction, no scatter correction was done and no information about the bed was used.

Figures 9 and 10 show the activity and attenuation reconstructions from the clinical data, respectively. In this study we used the CT-based scatter and bed attenuation values during MLAA reconstructions. The activity reconstructed from OSEM with CT-based attenuation correction and the one of MLAA are shown in figure 9 and the CT attenuation image and the reconstructed MLAA attenuation image are shown in figure 10.

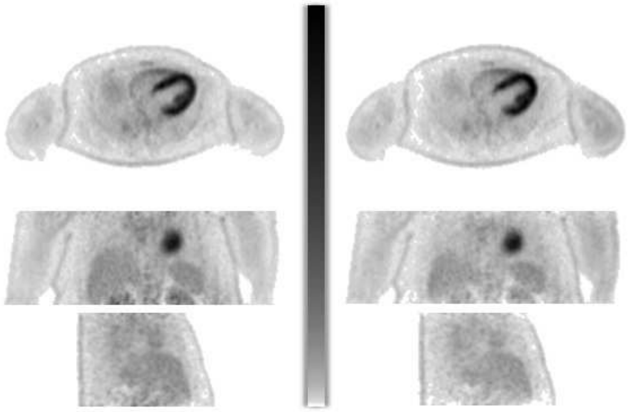

Fig. 9. Transaxial (top), coronal (center) and sagittal (bottom) view of the activity corrected with CT-based attenuation (left) and the activity reconstructed with MLAA (right) and CT-based scatter and bed correction. The MLAA image was smoothed with a 3D Gaussian with 6 mm FWHM to match approximately the resolution of the standard reconstruction. The vertical bar represents the gray level lookup table.

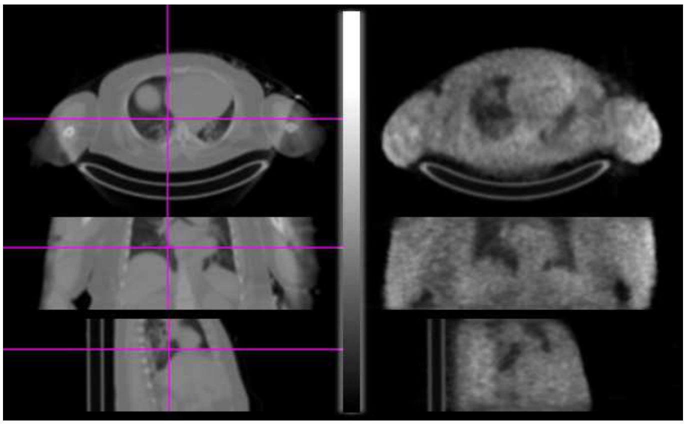

Fig. 10. Transaxial (top), coronal (center) and sagittal (bottom) view of the CT-based attenuation image (left) and attenuation image reconstructed with MLAA (right) from the emission data and CT-based scatter and bed correction. The MLAA image was smoothed with a 3D Gaussian with 6 mm FWHM. The vertical bar represents the gray level lookup table.

The two activity reconstructions shown in figure 9 look visually very similar and do not show obvious signs of cross-talk. Looking at the attenuation reconstruction of MLAA in figure 10, a good lung-tissue discrimination is observed. The algorithm has also been able to produce a fairly good estimate of the patient body contour making use of the tracer uptake in the entire body. However, the attenuation values are slightly elevated near the heart. This is probably due to significantly higher activity uptake in the heart, but further analysis is needed.

Figure 10 also shows that the MLAA attenuation reconstructions suffer less from truncation artifacts. This is partly because the CT scanner uses a slightly smaller FOV compared to the PET scanner of the mCT, and because iterative algorithms handle truncation better than analytic reconstructions. In this comparison, the portion of the liver visible in the lung of the patient is slightly different, which we attribute to the breathing motion during acquisition.

Figure 11 shows the activity and attenuation reconstructions from the clinical data without any CT-based compensation for scatter or attenuation values outside the patient boundary. As before, the reconstructions seem to be free of activity and attenuation cross-talk. However, in this MLAA reconstruction the activity is overestimated. This is associated to the excess attenuation in the attenuation image due to the over-estimation of the patient boundary.

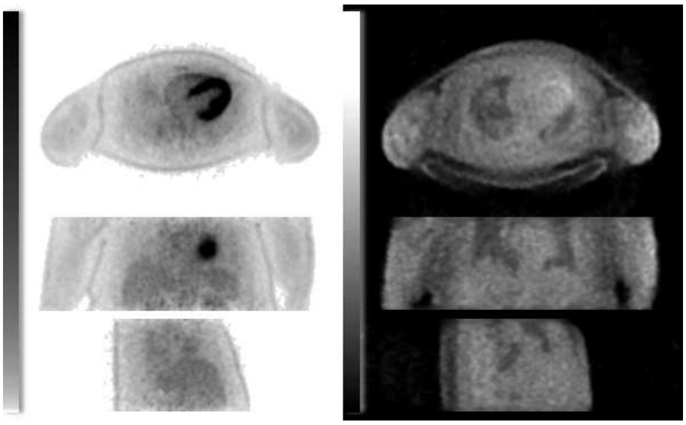

Fig. 11. Transaxial (top), coronal (center) and sagittal (bottom) view of activity (left) and attenuation (right) reconstructed with MLAA without any CT-based scatter and bed correction. The MLAA images were smoothed with a 3D Gaussian with 6 mm FWHM. The vertical bars represent the gray level lookup table for activity and attenuation.

The attenuation reconstruction of figure 11 shows that MLAA has been able to make a useful reconstruction of the attenuation medium but with less lung-tissue contrast than before. It has also been able to reconstruct the portion of the bed which lies inside the convex hull of the region containing activity. However, the boundary of the patient has been slightly over-estimated (region above the patient) which is mainly due to scatter.

IV. DISCUSSION

Simultaneous reconstruction of attenuation and activity in SPECT and non-TOF PET has been investigated by many groups, and was found to be a very ill-posed problem. Previous studies have shown that the use of time-of-flight reduces the sensitivity of the PET reconstruction to attenuation correction errors. The study presented here reveals that time-of-flight information has the ability to stabilize the joint estimation problem, and may therefore enable quantitative PET imaging without relying on transmission scans or other anatomical imaging procedures. Estimating the attenuation from the emission data has the advantage that it ensures a correct match with respect to photon energy and patient position, and probably a good match in the presence of motion blurring (e.g. heart beat, breathing). In practice, the method could prove useful in mitigating the problem of PET - CT registration when misalignment is an issue. When the PET data are compensated for attenuation based on the CT, the boundaries of a misaligned CT propagate into the PET image, affecting the subsequent registration. Attenuation correction independent of the CT may help to solve this problem.

As suggested by our experiments, and as proven by the theoretical analysis in [26], the TOF PET data enable the estimation of the attenuation sinogram up to a constant term, and therefore the estimation of the activity up to a constant factor. It is anticipated that in most applications, this constant can be determined in a fairly straightforward way by imposing the known attenuation value of tissue to a segmented portion of the attenuation image. An alternative way would be to combine the method with full or partial transmission information, which could e.g. be obtained by adding transmission source(s) in the field of view [34].

The PET emission data provide no (or at least incomplete) information about attenuation along LORs that do not intersect a region containing a significant amount of radioactive tracer. Many tracers, including ^{18}F-FDG, show uptake in the entire body. For such tracers, it is valid to assume that the attenuation along LORs without activity is zero everywhere. In our experiments, we have applied a prior encouraging the assignment of zero attenuation to such regions. It should be noted that reconstruction of the attenuation image outside the activity region has a slower convergence rate than the reconstruction of the attenuation image inside the activity region, even in the absence of the background prior. For these reasons, adding the effect of additional attenuating medium, specifically the bed, to the attenuation reconstruction instead of reconstructing the bed along with the unknown attenuation medium would be a more reasonable and practical approach.

The PET emission data are always noisy so in addition to the background prior, we use a smoothing Markov prior [31] in the attenuation image and a small amount of post-smoothing in the activity image. Many other priors have been proposed for emission and transmission tomography. Evaluation of such priors for regularization of this joint estimation problem is a topic for further research.

In both the 3D phantom study and the clinical study, we do not compensate for any scatter in the measurements and still are able to achieve reasonable reconstructions. We believe that given these scatter un-compensated reconstructions, it is possible to make an estimate of the scatter and refine the final activity and attenuation reconstructions in an additional step. In the clinical patient study, the patient was injected with a non-specific tracer that has a detectable accumulation in all tissues. This made attenuation reconstruction with roughly the true boundary possible. For more specific tracers that do not dissipate to the entire body, reconstruction of the attenuation image with the correct boundary might prove to be more difficult. The use of external sources [34] can help in these situations.

V. CONCLUSION

In this paper, the feasibility of simultaneous activity and attenuation reconstruction from the measurement data was investigated for a time-of-flight system. The MLAA algorithm, which makes alternated updates to the activity and attenuation images by means of the existing MLEM and MLTR algorithms, was used for this purpose.

The feasibility of this approach was verified for 2D and 3D phantom studies as well as for a clinical study. It was found that the utilization of time-of-flight information in simultaneous reconstructions eliminates the problem of activity and attenuation cross-talk. However, to ensure quantitative accuracy, limited prior knowledge is still required, because the solution is only determined up to a constant.

It was shown that as the time resolution of the TOF system increases, the convergence improves as well. The joint ML reconstruction was found to be robust to noise in the emission sinogram.

VI. APPENDIX

The background prior we use is an absolute intensity prior favoring zero attenuation in the background. Since in each iteration the gradient of the prior is added to the one of the likelihood, here we only express the gradient of this background prior. Defining $\partial\mathcal{BG}/\partial\mu_j$ as the gradient of the prior we set this value to be,

$$\frac{\partial \mathcal{BG}}{\partial \mu_j} = \frac{-W_{\mathcal{BG}}}{\sigma^2}\frac{|\mu_j(\mu_j-\mu_T)|}{\mu_j+c\mu_T}, \quad j=1,...,J \tag{19}$$

where μ_j is the attenuation value at voxel j, $W_{\mathcal{BG}}$ defines the prior strength, μ_T is our expected tissue attenuation, σ is a standard deviation measure of tissue which was set to μ_T and parameter c is a skewness parameter. It can be seen that the prior has no effect for voxels with zero or tissue attenuation values. Parameter c is used to adjust the prior strength to have a greater effect for attenuation values near zero than attenuation values close to μ_T. In the simulations we used $c = 0.05$ and replaced $\partial^2\mathcal{BG}/\partial\mu_j^2$ by its upper limit $-W_{\mathcal{BG}}/c\sigma^2$.

REFERENCES

[1] PE Kinahan, DW Townsend, T Beyer *et al.*, “Attenuation correction for a combined 3D PET/CT scanner”, *Med Phys*, 1998, 25(10):2046-2053.

[2] H Zaidi, BH Hasegawa, “Attenuation correction strategies in Emission Tomography”, in *Qualitative analysis in nuclear medicine imaging*, H Zaidi, Springer Science + Business Media Inc. 2006

[3] M Defrise, PE Kinahan, CJ Michel, “Image Reconstruction algorithms in PET”, in *Positron Emission Tomography*, DL Bailey, DW Townsend, PE Valk, MN Maisey Springer-Verlag London Limited 2005

[4] Y Censor, DE Gustafson, A Lent, H Tuy, “A new approach to the emission computerized tomography problem: simultaneous calculation of attenuation and activity coefficients”, *IEEE Trans Nucl Sci*, 1979, 26(2):2775-2279.

[5] F Natterer, “Determination of tissue attenuation in emission tomography of optically dense media”, *Inverse Problems*, 1993, 9(6):731-736.

[6] A Welch, R Clack, F Natterer *et al.*, “Toward accurate attenuation correction in SPECT without transmission measurements”, *IEEE Trans Med Imaging*, 1997, 16(5):532-541.

[7] J Nuyts, P Dupont, S Stroobants *et al.*, “Simultaneous maximum a-posteriori reconstruction of attenuation and activity distributions from emission sinograms”, *IEEE Trans Med Imaging*, 1999, 18(5):393-403.

[8] AV Bronnikov, “Reconstruction of attenuation map using discrete consistency conditions”, *IEEE Trans Med Imaging*, 2000, 19(5):451-462.

[9] H Kudo, H Nakamura, “A new approach to SPECT attenuation correction without transmission measurements”, *IEEE Nucl Sci Symp Conf Record*, Oct-2000, 2(13):58-62.

[10] VY Panin, GL Zeng, GT Gullberg, “A method of attenuation map and emission activity reconstruction from emission data”, *IEEE Trans Nuc. Science*, 2001, 48(1):131-138.

[11] A Krol, JE Bowsher, SH Manglos *et al.*, “An EM algorithm for estimating SPECT emission and transmission parameters from emission data only”, *IEEE Trans Med Imaging*, 2001, 20(3):218-232.

[12] F Crepaldi, A De Pierro, “Activity and attenuation recovery from activity data only in emission computed tomography”, *IEEE Trans Nuc. Science*, 2007, 54:100-106.

[13] CM Laymon and JE Bowsher, “A log likelihood based method for recovery of localized defects in PET attenuation-correction images”, *IEEE Nucl Sci Symp Conf Record*, Oct 2004, 2710-2714.

[14] J Nuyts, C Michel, M Fenchel *et al.*, “Completion of a truncated attenuation image from the attenuated emission data”, *IEEE Nucl Sci Symp Conf Record*, Oct-Nov 2010, 2123-2127.

[15] A Salomon, A Goedicke, B Schweizer *et al.*, “Simultaneous reconstruction of activity and attenuation for PET/MR”, *IEEE Trans Med Imaging*, 2011, 30(3):804-813.

[16] WW Moses, “Time of Flight in PET revisited”, *IEEE Trans Med Imaging*, 2003, 50(5):1325-1330.

[17] M Conti, B Bendriem, M Casey *et al.*, “First experimental results of time-of-flight reconstruction on an LSO PET scanner”, *Phys Med Biol* 2005, 50(19):4507-4526.

[18] S Surti, A Kuhn, ME Werner *et al.*, “Performance of Philips Gemini TF PET/CT scanner with special consideration for its time of flight imaging capabilities”, *J Nucl Med* 2007, 48(3):471-480.

[19] BW Jakoby, Y Bercier, M Conti *et al.*, “Physical and clinical performance of the mCT time-of-flight PET/CT scanner”, *Phys Med Biol* 2011, 56(8):2375-2389.

[20] M Conti, “Why is TOF PET reconstruction a more robust method in the presence of inconsistent data?”, *Phys Med Biol* 2011, 56(1):155-168.

[21] W Wang, Z Hu, EE Gualtieri *et al.*, “Systematic and distributed Time-of-Flight List mode PET reconstructions”, *IEEE Nucl Sci Symp Conf Record* Oct-Nov 2006, 1715-1722.

[22] K Vunckx, L Zhou, S Matej *et al.*, “Fisher Information-based Evaluation of Image quality for Time-of-Flight PET”, *IEEE Trans Med Imaging*, 2010, 29(2):311-321.

[23] LS Shepp, Y Vardi, “Maximum likelihood reconstruction for emission tomography”, *IEEE Trans Med Imaging*, 1982, 1(2):113-122.

[24] JA Fessler, EP Ficaro, NH Clinthorne *et al.*, “Grouped-Coordinate Ascent Algorithms for Penalized-Likelihood Transmission Image Reconstruction”, *IEEE Trans Med Imaging* 1997, 16(2):166-175.

[25] J Nuyts, B De Man, P Dupont *et al.*, “Iterative reconstruction for helical CT: a simulation study”, *Phys Med Biol*, 1998, 43(4):729-737.

[26] M Defrise, A Rezaei, J Nuyts, “Time-of-flight PET data determine the attenuation sinogram up to a constant”, *Phys Med Biol*, 2012, 57(4):885-899.

[27] JA Fessler, WL Rogers, “Spatial resolution properties of Penalized-likelihood image reconstruction: Space-Invariant Tomographs”, *IEEE Trans Med Imaging*, 1996, 5(9):1346-1358.

[28] Q Li, E Asma, J Qi *et al.*, “Accurate estimation of the fisher information matrix for the pet image reconstruction problem”, *IEEE Trans Med Imaging*, 2004, 23(9):1057-1064.

[29] M Defrise, V Panin, C Michel *et al.*, “Continuous and Discrete Data Rebinning in Time-of-Flight PET” *IEEE Trans Med Imaging*, 2008, 27(9):1310-1322

[30] FH Fahey, “Data aquisition in PET imaging”, *J Nucl. Med. Technol*, 2002, 30(2):39-49.

[31] J Nuyts, D Beque, P Dupont *et al.*, “A Concave prior penalizing relative differences for maximum-a-posteriori reconstruction in emission tomography”, *IEEE Trans Nuc. Science*, 2002, 49(1):56-60.

[32] “www.spect.com/pub/NEMA_IEC_Body_Phantom_Set.pdf”

[33] CC Watson, “Extension of single scatter simulation to scatter correction of time-of-flight PET”, *IEEE Trans Nuc. Science*, 2007, 54(5):1679-1686.

[34] P Mollet, K Keereman, S Vandenberghe, “Experimental evaluation of simultaneous emission and transmission imaging using TOF information” *IEEE Nucl Sci Symp Conf Record*, Oct 2011, 2976-2980.